

pubs.acs.org/JPCL Letter

Resonant Stimulated X-ray Raman Spectroscopy of Mixed-Valence Manganese Complexes

Stefano M. Cavaletto, Daniel R. Nascimento, Yu Zhang, Niranjan Govind, and Shaul Mukamel*



Cite This: J. Phys. Chem. Lett. 2021, 12, 5925-5931



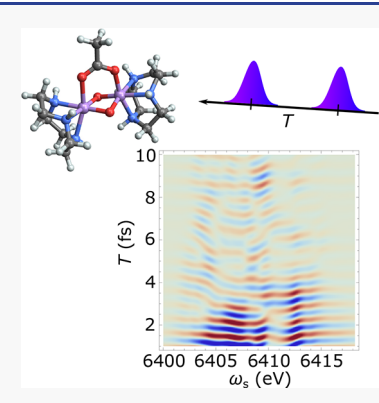
ACCESS

Metrics & More

Article Recommendations

Supporting Information

ABSTRACT: Resonant stimulated X-ray Raman spectroscopy of the bimetallic $[Mn^{III}Mn^{IV}(\mu-O)_2(\mu-OAC)(tacn)_2]^{2+}$ manganese complex is investigated in a simulation study. Essential biological processes, including water oxidation in photosynthesis, involve charge transfer between manganese sites of different oxidation states. We study a prototypical binuclear mixed-valence transition-metal complex with two Mn atoms in different oxidation states surrounded by ligand structures and employ a pump—probe sequence of resonant X-ray Raman excitations to follow the charge transfer occurring in the molecule. This allows us to generate and monitor valence-electron wave packets at selected regions in the molecule by exploiting element-specific core-excited states. A two-color protocol is presented, with pump and probe pulses tuned to the Mn and N K-edges. A natural orbital decomposition allows the visualization of the electron dynamics underlying the signal.



anganese plays a decisive role in chemical and biological anganese plays a decisite loss processes. It is an essential constituent of enzymes involved in fundamental biological reactions, such as the breakdown of superoxide and water oxidation in photosynthesis.2 In photosystem II, a protein present in plants, algae, and cyanobacteria, the role of Mn active sites has been the object of intense experimental scrutiny. In this protein, Mn₄Ca clusters have been shown to catalyze light-induced electrontransfer reactions leading to water oxidation while cycling through different oxidation states.3 In order to understand these elementary processes and the role played by manganese, it is thus necessary to probe the charge transfer occurring between separate Mn sites of different oxidation states. Electron-paramagnetic-resonance (EPR) spectroscopy has been utilized to study Mn complexes, but with limitations on the ground-state spin of the complexes it can be applied to.^{4,5} X-ray absorption and emission spectroscopies⁶ have also been investigated, providing access to the core- and valence-excited states in the systems, but with limited access to their

With recent advances in the generation of short, coherent X-ray pulses by high-order harmonic generation and free-electron lasers (FELs), 7-10 it is now possible to extend multidimensional nonlinear spectroscopy to higher frequencies from XUV up to the hard-X-ray regime. 11 These spectroscopy techniques employ sequences of pulses with suitably set frequencies and delays. They were developed in nuclear magnetic resonance spectroscopy in the radio-wave regime to access correlations between different nuclear spins and then extended to the infrared and visible domain, enabling breakthrough studies of vibrational dynamics in molecules. Because of their short

duration and broad bandwidth, coherent X-ray pulses can directly probe electron dynamics involving several excited states on their natural ultrafast time scales. Furthermore, core-excited states have element-specific transition energies lying in the X-ray domain. Using X-ray pulses resonant to different core-excited states provides access to the correlations between excitation events localized at different atoms in the molecule. Multidimensional nonlinear X-ray spectroscopy thus offers enhanced spatial resolution of ultrafast molecular dynamics.

Here, we apply resonant stimulated X-ray Raman spectroscopy (SXRS) $^{12-15}$ to monitor the electronic dynamics of the binuclear mixed-valence transition-metal complex [MnIIIMnIV(μ -O) $_2$ (μ -OAC)(tacn) $_2$] $^{2+16}$ shown in Figure 1a, with two Mn atoms in different oxidation states surrounded by ligand structures containing C, N, and O atoms. Resonant SXRS is a multidimensional nonlinear X-ray technique employing two resonant X-ray pulses (Figure 1b) separated by a variable time delay and inducing two resonant Raman excitations. The elementary steps involved in SXRS were recently demonstrated experimentally with X-ray FEL pulses, enabling stimulated X-ray emission in Ne 17 and Mn complexes and resonant X-ray Raman excitation in Ne 19,20 and NO gases. In SXRS, each pulse induces a Raman excitation between ground and valence-excited states via a

Received: April 13, 2021 Accepted: June 17, 2021 Published: June 22, 2021





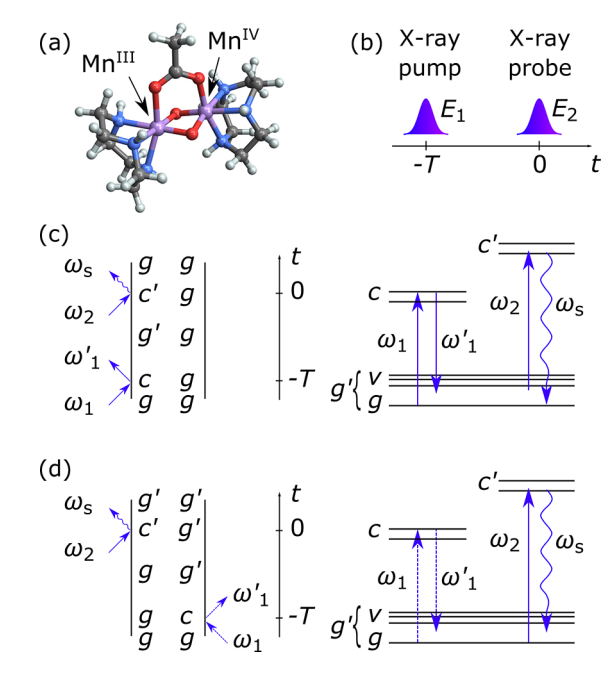


Figure 1. (a) Structure of the binuclear Mn complex $[Mn^{III}Mn^{IV}(\mu-O)_2(\mu-OAC)(\tan n)_2]^{2+}$, with Mn^{III} (purple, left) and Mn^{IV} (purple, right) centers with different oxidation states and ligand structures containing C (gray), N (blue), O (red), and H (white) atoms. (b) Pulse sequence in resonant stimulated X-ray Raman spectroscopy and (c and d) ladder diagram (left) and level scheme (right) of the two contributing pathways.

resonant transition through selected core-excited states, as depicted in Figure 1c,d. By tuning the pump and the probe pulses to the transition energies of the core states of different elements, resonant SXRS can generate a wave packet and monitor its evolution at different regions in the molecule with spatial selectivity. We study two-color pump—probe pulse sequences by tuning the pump and probe pulses to the transition energies of Mn or N 1s core-excited states. Different wave packets are generated by pump pulses tuned to different K-edges in the molecule. By additionally varying the color of the probe pulse, dynamical information on the underlying molecular orbitals, localized at the metals or at the ligand, is extracted.

The resonant SXRS setup is sketched in Figure 1b. A broadband X-ray pump pulse, with central frequency ω_{10} and spectral envelope $\mathcal{E}_1(\omega - \omega_{10})$, excites the molecule initially in its ground state g. The pulse generates a coherent superposition of valence states ν by a resonant Raman process via the core states c. The ensuing evolution of the molecular wave packet, described by the coherence ho_{vg} between ground and valence-excited states, is monitored after a time delay T by a probe pulse $\mathcal{E}_2(\omega-\omega_{20})$ of central frequency ω_{20} , inducing a second Raman process through the core states c'. Measuring the frequency-dispersed absorption of the transmitted probe pulse $\tilde{\mathcal{E}}_2$ at varying time delays T results in the frequency- and time-resolved signal $S(\omega_s, T) = S_{LA}(\omega_s) + S_{GSB}(\omega_s) +$ $S_{\rm SXRS}(\omega_s, T)$. The first term $S_{\rm LA}(\omega_s)$ is the linear X-ray absorption near-edge structure (XANES) spectrum, determined by the first-order response of the molecule and involving two interactions along the $g \to c \to g$ pathway. Additional ground-state bleaching (GSB) $S_{\text{GSB}}(\omega_s)$ and the time-dependent SXRS signal $S_{\text{SXRS}}(\omega_s, T)^{22}$ are third-order contributions in the presence of the pump pulse \mathcal{E}_1 , involving four interactions along the $g \to c \to g' \to c' \to g$ pathway. The two ladder diagrams and level schemes contributing to both GSB (g'=g) and SXRS $(g'=\nu)$ are displayed in Figure 1c,d. More details are provided in the Supporting Information (sections S1 and S4). We neglect third-order contributions in which the pump pulse induces two upward excitations to a cc' state. Such states decay on (sub)femtosecond time scales, much faster than the gg' coherence involved in SXRS, and do not contribute to the pump—probe experiment for sufficiently long time delays. We further assume an optically thin medium, where propagation effects can be neglected.

The SXRS signal features pairs of peaks, centered at ω_s = $\omega_{c'g}$ (Figure 1c) and $\omega_s = \omega_{c'v}$ (Figure 1d). Their line shapes vary with T, reflecting the evolution of the coherences $\rho_{\nu\sigma}$ encountered by the probe pulse for different time delays, and thus providing information on the valence states and their couplings to different core-excited states. In the following simulations, we assume coherent pulses with a Gaussian spectral profile, $\tilde{\mathcal{E}}_i(\omega) = \tilde{\mathcal{E}}_{i0} e^{-\omega^2/(2\sigma_i^2)}$, $i \in \{1, 2\}$, with peak strengths $\tilde{\mathcal{E}}_{i0}$ and bandwidths $\sigma_i = 7.3$ eV. This corresponds to Gaussian temporal envelopes $\mathcal{E}_i(t) = \mathcal{E}_{i0} e^{-\sigma_i^2 t^2/2}$, with $\mathcal{E}_{i0} = \tilde{\mathcal{E}}_{i0} \sigma_i / \sqrt{2\pi}$ and peak intensities $I_{i0} = |\mathcal{E}_{i0}|^2 / (8\pi\alpha)$ in terms of the fine-structure constant α . Atomic units are used unless otherwise stated. The XANES and SXRS signals are linear in the peak intensities of the pulses involved. In the following, we present results where the signals are normalized by the peak strength of the pulses, i.e., we set $\tilde{\mathcal{E}}_{i0}=1$ au corresponding to peak pulse intensities of $I_{i0} = 4 \times 10^{14} \text{ W/cm}^2$. All signals are rotationally averaged²³ in order to account for randomly oriented molecules.

We apply two-color pump–probe SXRS to monitor the electronic dynamics of the binuclear Mn complex [Mn^{III}Mn^{IV}(μ -O)₂(μ -OAC)(tacn)₂]²⁺¹⁶ in Figure 1a. Linear response time-dependent density functional theory (LR-TDDFT) simulations allow us to determine the transition energies $\omega_{cg'}$ and dipole couplings $V_{cg'}$, and assign the core and valence states to the underlying contributing molecular orbitals. The decay of the Mn and N core-excited states is modeled by the decay rates $\gamma_{cg'}=0.58~{\rm eV}^{25}$ and $\gamma_{cg'}=0.2~{\rm eV},^{22}$ respectively. Valence-state line widths are set to $\gamma_{vg}=0.05~{\rm eV}$ in order to model the effects of decoherence and decay stemming, e.g., from nuclear motions. Further information about the calculations is provided in Computational Details.

Figure 2 shows the linear-absorption and SXRS spectra for broadband pump and probe X-ray pulses tuned to the Mn K-edge. The linear-absorption spectrum in Figure 2a involves two resonant interactions and is thus determined by products of two dipole couplings V_{cg} , where c labels a Mn core-excited state. The spectrum features four clearly separated peaks, which we assign via the orbital decomposition shown in Figure 3. The first peak has two main contributions from two core states, at $\omega_{cg} = 6407.9$ eV and $\omega_{cg} = 6409.6$ eV. These states involve metal-to-metal transitions of a Mn^{III} (Figure 3a) and a Mn^{IV} (Figure 3b) core electron, respectively. In both cases, the core electron moves to unoccupied orbitals around both metallic centers. The second peak in Figure 2a has a strong contribution from a state at $\omega_{cg} = 6412.6$ eV, related to a metal-to-metal transition of a core electron at the Mn^{III} site (Figure 3c). The two higher-frequency peaks in Figure 2a are associated with metal-to-ligand transitions, where a metal

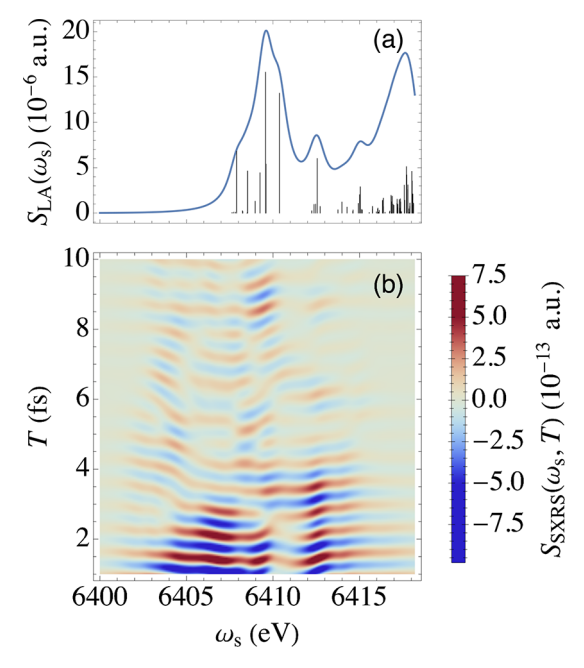


Figure 2. XANES and SXRS spectra for broadband pump and probe X-ray pulses tuned to the Mn K-edge. Broadband pump $\tilde{\mathcal{E}}_{10}(\omega-\omega_{10})$ and probe $\tilde{\mathcal{E}}_{20}(\omega-\omega_{20})$ pulses are assumed, with $\omega_{10}=\omega_{20}=6412$ eV, $\sigma_1=\sigma_2=7.3$ eV, and $\tilde{\mathcal{E}}_{10}=\tilde{\mathcal{E}}_{20}=1$ au. (a) Rotationally averaged linear-absorption spectrum $S_{\rm LA}(\omega_s)$ in the absence of the pump pulse. The black vertical lines are centered around the core-state transition energies ω_{cg} from the ground state g, normalized by the associated, rotationally averaged dipole couplings $|V_{cg}|^2$. (b) Rotationally averaged pump-probe SXRS spectrum $S_{\rm SXRS}(\omega_{sg},T)$.

core electron moves to unoccupied molecular orbitals around the ligand.

In contrast to linear absorption, the SXRS spectrum of Figure 2b involves four resonant interactions: two induced by the pump and two by the probe pulse. This is associated with products of four dipole couplings $V_{cg'}$ and is reflected in the

different strength of the signals in Figure 2a,b. The two highlighted pathways in panels c and d of Figure 1 lead to the emission of a photon at frequencies centered on $\omega_{c'\sigma}$ and $\omega_{c'\nu}$ respectively. As a result, for every core-excited state c', the SXRS signal features couples of peaks centered on $\omega_s = \omega_{c'g}$ and $\omega_s = \omega_{c'v'}$ at frequencies separated by the transition energy ω_{vg} of the valence-excited states generated during the resonant Raman excitation. The SXRS signal is therefore also present at $\omega_{\rm s}$ < 6407 eV, in frequency regions in which the linearabsorption signal is absent. Interestingly, the SXRS spectrum does not feature any peaks at $\omega_s > 6415$ eV. This reveals that the higher-frequency core states, contributing to the linearabsorption signal and involving metal-to-ligand transitions, do not couple effectively to the valence states in the molecule, i.e., $V_{c\nu} \ll V_{cg}$. The time-delay dependence of the SXRS line shapes in Figure 2b and their oscillatory behavior reflect the free evolution $e^{-i\omega_{vg}T}e^{-\gamma_{vg}T}$ of the valence-excited states generated by the pump and the phase of the valence electronic wave packet encountered by the probe pulse. As a result, the SXRS spectrum oscillates between positive and negative signals, associated with photon absorption and emission, respectively. The valence states contributing to the SXRS signal, which are generated when the core hole produced by X-ray absorption is filled by electrons from previously occupied molecular orbitals, are highlighted in Figure 3.

In order to implement an effective two-color scheme, we also consider additional resonant excitations to N core-excited states, as shown in Figure 4. The linear-absorption spectrum at the N K-edge is displayed in Figure 4a. The spectrum is determined by the product of two dipole couplings V_{cg} , where c is a N core-excited state. The different strength of the signal compared to the Mn spectrum of Figure 2a is thus a consequence of the amplitude of the Mn and N dipole couplings, which differ by approximately 2 orders of magnitude. The spectrum features four main peaks, which we assign via the orbital decomposition of Figure 3. Strong contributions to the first two peaks are due to states at ω_{cg} = 389.2 eV and ω_{cg} = 389.9 eV, involving ligand-to-metal transitions of N core electrons localized on the left (Figure 3a)

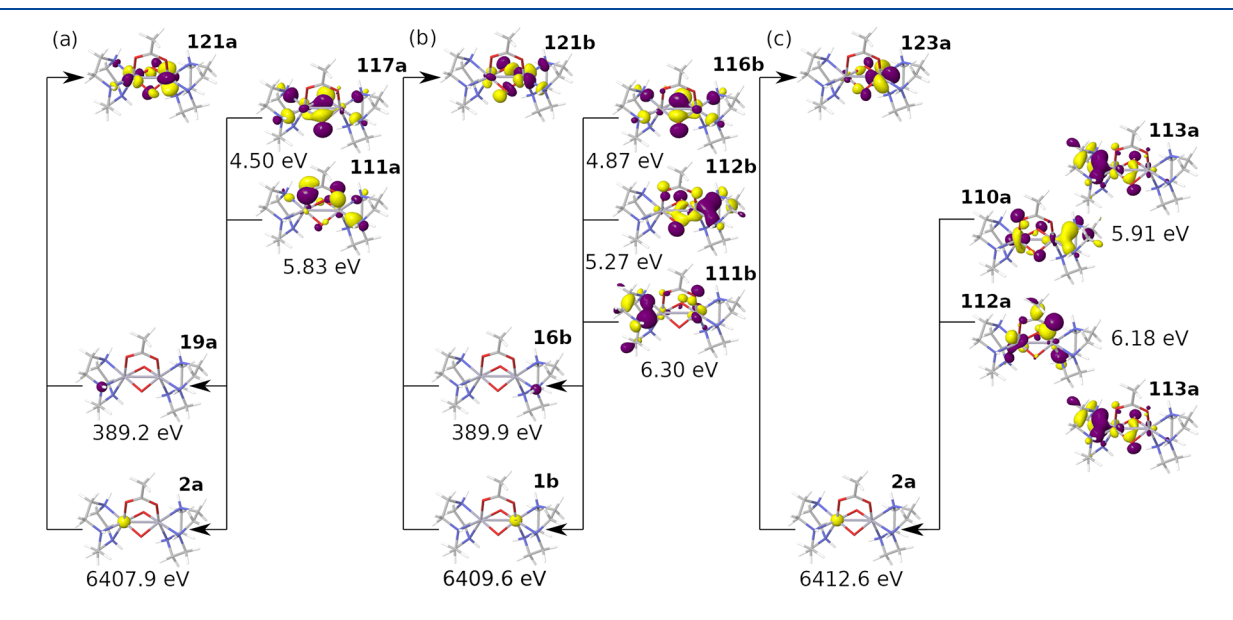


Figure 3. Orbital decomposition of the Mn and N core- and valence-excited states contributing to the linear-absorption and SXRS signals in Figures 2, 4, and 5. Orbital contributions to the relevant roots within each excited-state manifold are provided in Table S1.

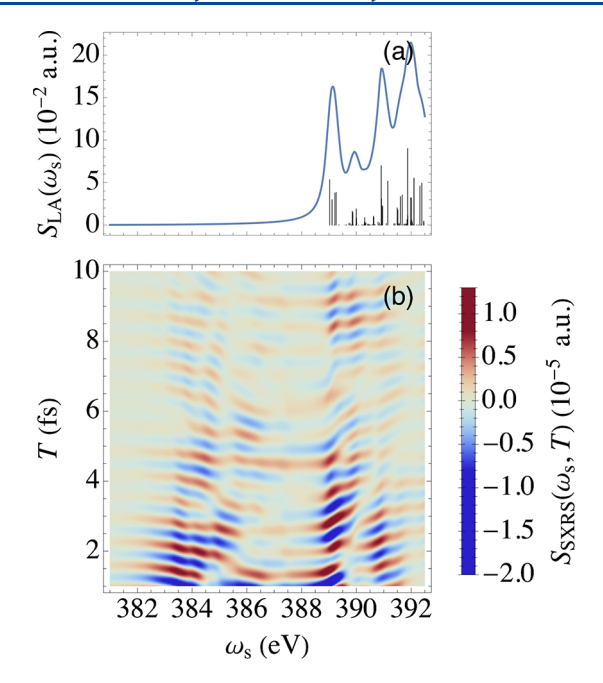


Figure 4. XANES and SXRS spectra for broadband pump and probe X-ray pulses tuned to the N K-edge. Broadband pump $\tilde{\mathcal{E}}_1(\omega-\omega_{10})$ and probe $\tilde{\mathcal{E}}_2(\omega-\omega_{20})$ pulses are assumed, with $\omega_{10}=\omega_{20}=387.5$ eV, $\sigma_1=\sigma_2=7.3$ eV, and $\tilde{\mathcal{E}}_{10}=\tilde{\mathcal{E}}_{20}=1$ au. (a) Rotationally averaged linear-absorption spectrum $S_{\rm LA}(\omega_{\rm s})$ in the absence of the pump pulse. The black vertical lines are centered around the corestate transition energies $\omega_{\rm cg}$ from the ground state g, normalized by the associated, rotationally averaged dipole couplings $|V_{\rm cg}|^2$. (b) Rotationally averaged pump–probe SXRS spectrum $S_{\rm SXRS}(\omega_{\rm sr},T)$.

or on the right ligand (Figure 3b), respectively. These N core electrons partly move to the same unoccupied orbitals previously identified for X-ray excitations resonant to the Mn core. The SXRS spectrum in Figure 4, with broadband pump and probe pulses both resonant to the N core, exhibits the same structure identified above, with couples of peaks centered at $\omega_{c\sigma}$ and $\omega_{c\sigma}$ whose line shapes vary with T as a result of the evolution of the valence-excited states. Here and in the following, we assume fixed pulse bandwidths of $\sigma_i = 7.3$ eV for the resonant excitation of both Mn and N core-excited states, although existing X-ray FEL sources have pulse bandwidths which scale with the photon energy. We notice, however, that such broad bandwidths are not required for the resonant excitation of N core-excited states, as apparent from the range of the ω_s axis in Figure 4. Our results would not change significantly by assuming a narrower bandwidth for the pulses tuned to the N K-edge.

The correlations between core and valence states accessed by the SXRS signal are more clearly highlighted by computing the Fourier transform of $S_{\rm SXRS}(\omega_s,T)$ over the time delay T, $\tilde{S}_{\rm SXRS}(\omega_s,\Omega)=2|\int_0^\infty S_{\rm SXRS}(\omega_s,T)\,{\rm e}^{i\Omega T}\,{\rm d}T|$, which is a function of ω_s and of the frequency Ω conjugated to T. Because of the dependence of $S_{\rm SXRS}(\omega_s,T)$ on the valence-state dynamics, ${\rm e}^{-i\omega_{v_g}T}\,{\rm e}^{-\gamma_{v_g}T}$, the Fourier transform $\tilde{S}_{\rm SXRS}(\omega_s,\Omega)$ features peaks at the transition energies $\Omega=\omega_{v_g}$ of the valence-excited states generated by the resonant X-ray Raman excitation. The two-dimensional SXRS signal $\tilde{S}_{\rm SXRS}(\omega_s,\Omega)$ is exhibited in Figure 5 for different two-color pulse sequences, with pump and probe pulses tuned to the Mn or to the N K-edges of $[{\rm Mn}^{\rm III}{\rm Mn}^{\rm IV}(\mu-{\rm O})_2(\mu-{\rm OAC})({\rm tacn})_2]^{2+}$, respectively. In all panels, the peaks centered at $\Omega=\omega_{v_g}$ reveal the transition energies of the valence

states accessed by the X-ray pump Raman excitation, and their couplings to the core-excited states can be read off the ω_s axis via the couple of peaks centered at $\omega_s = \omega_{cg}$ or $\omega_s = \omega_{cv}$. This property appears in all panels but is especially prominent in Figure 5c,d. Because of the many close-lying core and valence states involved in the excitation, the peaks displayed in Figure 5 present some asymmetric dispersive-type features. When the core states are very close to each other, as shown by the black vertical lines in Figures 2a and 4a, the sum and interference of their contributions can lead to these complex line shapes. Additional time-independent contributions from GSB would appear as peaks centered at $\Omega=0$ eV and are not displayed in Figure 5.

Figure 5a is the Fourier transform over *T* of the SXRS signal in Figure 2b, where both pump and probe pulses are tuned to Mn core-excited states. Two intense peaks can be distinguished at $\omega_s = 6412.6$ eV and $\Omega = 5.91$ eV or $\Omega = 6.18$ eV. The associated molecular orbitals are identified in the right column of Figure 3. Interestingly, even though these excitations are associated with a pathway through the Mn^{III} atom on the left side of the complex, the resulting valence states occupy both left and right regions. Other peaks can be identified also at ω_s = 6407.9 eV and ω_s = 6409.6 eV, associated with X-ray Raman excitations via Mn^{III} and Mn^{IV}, respectively. Nevertheless, the valence states reached via both pathways are not preferentially localized on either side of the complex, as confirmed by the orbital decomposition of Figure 3. This is a consequence of the similar chemical environments of the two Mn atoms, which introduces limited variations to the core excitation spectra. This property is nicely captured by a two-color SXRS scheme as shown in the Figure S1, where we employ narrower pump and probe pulses covering different Mn core-excited states. Independent of the color of the X-ray pump pulse, tuned around 6407 eV or 6410 eV, the SXRS signals display similar peaks along the Ω axis, which confirms that similar superpositions of valence states are generated despite tuning the X-ray pump pulse to different core-excited states. Thereby, two-color SXRS provides information on the delocalized nature of the valence states generated by X-ray Raman excitation and the associated molecular charge densities.

The spectral proximity of the metal-to-metal transitions at the Mn K-edge, especially between core states at 6407.9 and 6409.6 eV, renders it challenging to separately address the two metallic centers with two-color schemes. To extend the capabilities of two-color SXRS, in Figure 5b we display results obtained for a pump pulse tuned to the N K-edge and a probe pulse still tuned to the Mn K-edge. A comparison with Figure 5a immediately reveals the different superposition of valenceexcited states generated by this pathway. First, a stronger signal is obtained because of the two-order-of-magnitude larger dipole couplings $V_{c'o'}$ for N c' states. Second, the strengths of the peaks in Figure 5a,b clearly differ. Pumping at the Mn Kedge leads to a preferential coupling to valence states at Ω = 5.91 eV or Ω = 6.18 eV. In contrast, when the pump pulse is tuned to the N core states, the strongest spectral lines are associated with states at Ω = 5.27 eV or Ω = 5.83 eV. The twodimensional SXRS signal provides access to these different underlying couplings and thus to the preferential pathways through which a desired electronic wave packet of valenceexcited states can be generated.

When the color of the probe pulse is modified, SXRS allows one to access the couplings between valence- and different sets of core-excited states in the molecule. This is shown in Figure

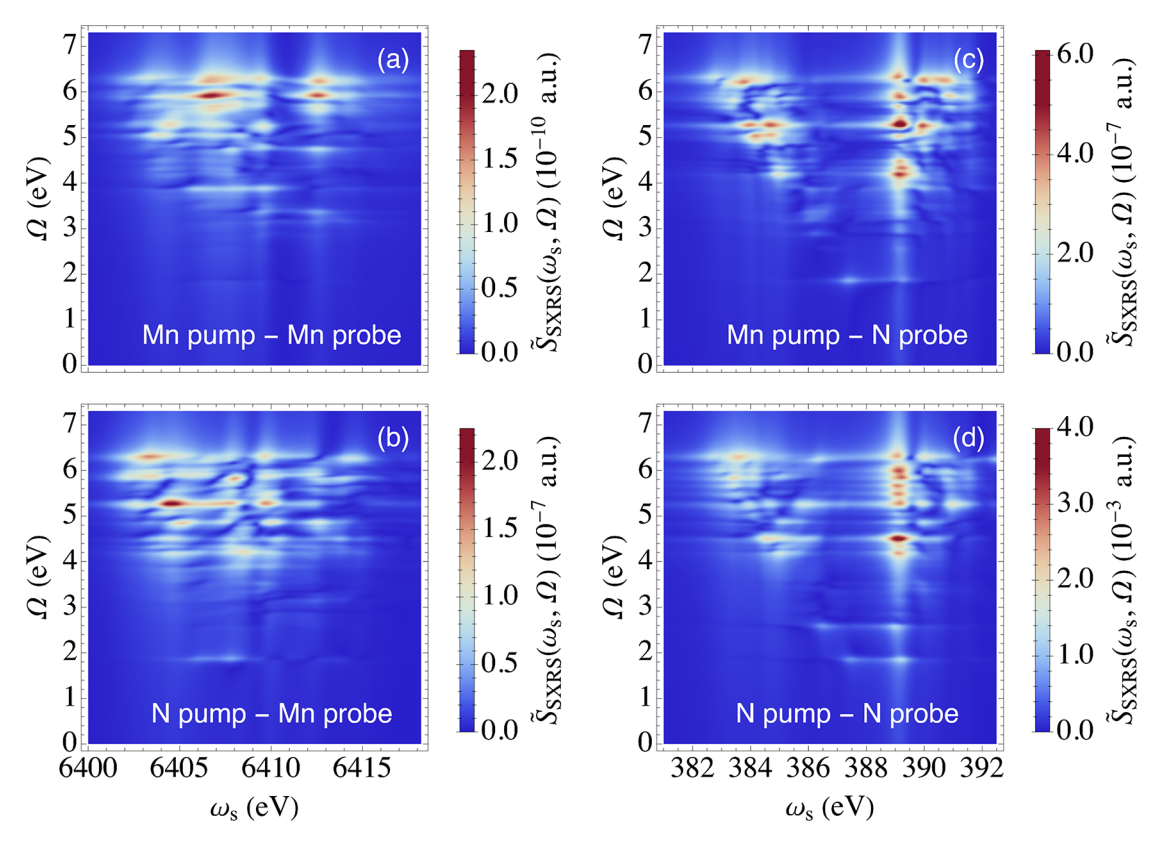


Figure 5. Rotationally averaged two-color SXRS spectra $\tilde{S}_{\text{SXRS}}(\omega_s, \Omega)$ with X-ray pulses tuned to the Mn and N K-edges of $[\text{Mn}^{\text{III}}\text{Mn}^{\text{IV}}(\mu\text{-O})_2(\mu\text{-OAC})(\text{tacn})_2]^{2+}$. Gaussian pump $\tilde{\mathcal{E}}_{10}(\omega-\omega_{10})$ and probe $\tilde{\mathcal{E}}_{20}(\omega-\omega_{20})$ spectral profiles are assumed, with bandwidths $\sigma_1=\sigma_2=7.3$ eV, peak strengths $\tilde{\mathcal{E}}_{10}=\tilde{\mathcal{E}}_{20}=1$ au, and central frequencies (a) $\omega_{10}=\omega_{20}=6412$ eV (pump and probe both tuned to the Mn K-edge), (b) $\omega_{10}=387.5$ eV and $\omega_{20}=6412$ eV (pump and probe tuned to the N and to the Mn K-edge, respectively), (c) $\omega_{10}=6412$ eV and $\omega_{20}=387.5$ eV (pump and probe tuned to the N K-edge, respectively), and (d) $\omega_{10}=\omega_{20}=387.5$ eV (pump and probe both tuned to the N K-edge).

5d, which presents the Fourier transform over T of $S_{\text{SXRS}}(\omega_{\text{s}}, T)$ in Figure 4b, with pump and probe pulses both tuned to the N K-edge. Because of the larger V_{cg^\prime} dipole couplings involving N core states, an increase in the signal strength is apparent in comparison to the previous panels. The spectrum reveals a significant number of valence-excited states coupling to the core-excited states lying around 389 eV. The valence states at energies lying between 4 eV and 5 eV appear more prominently in the SXRS signal of Figure 5d than in Figure 5a,b, indicating that they are more effectively excited by an X-ray pulse tuned to the N than to the Mn K-edge. This is also confirmed by Figure 5c, where the electronic wave packet stems from an X-ray Raman pump excitation passing through the Mn core. In such a case, the spectrum reveals that the valence states at ω_{vg} = 5.27 eV and ω_{vg} = 5.83 eV can be more efficiently excited via a Raman excitation exploiting the Mn core. Two-color SXRS can therefore access the pathways underlying resonant X-ray Raman processes and the information visualized by the orbital analysis of Figure 3.

For an experimental realization of the SXRS scheme proposed here, relevant parameters such as pulse intensities and density and size of the molecular sample will have to be properly set. Photoionization channels can cause population losses, which were not accounted for explicitly here. This can be especially relevant for X-ray pulses tuned to the N K-edge, as they can induce significant C 1s photoionization. The intensity of the X-ray pulses used will therefore have to be suitably optimized in order to minimize photoionization pathways. We notice that the strength of the measurable

signal, displayed in Figures 2, 4, and 5 for representative pump and probe intensities of $I_{i0} = 4 \times 10^{14}$ W/cm², scales linearly with I_{i0} . Decreasing the probe-pulse intensity in order to reduce photoionization effects will therefore not affect the relevant signal-to-background ratio, i.e., the ratio between the number of absorbed and incident probe-pulse photons in an experiment. In the Supporting Information (section S5), for representative experimental parameters, we estimate a signal-to-background ratio of ~2.5% for the Mn XANES signal of Figure 2a. Measurable signal-to-background ratios can then be obtained also for SXRS by a suitable choice of the experimental parameters. We stress that stimulated resonant X-ray Raman scattering, the building block of SXRS, was demonstrated in atomic neon 19,20 and in NO molecules 21 in the presence of photoionization channels.

In conclusion, we have applied resonant SXRS to investigate ultrafast electronic dynamics of mixed-valence Mn complexes. Two-color pump—probe sequences were employed to generate and monitor electronic wave packets at different positions in the molecule. A different superposition of valence-excited states can be generated by pump pulses tuned to element-specific Mn and N K-edges. Their dynamics and correlations were accessed by a subsequent X-ray probe pulse tuned to the same or to a different core. This provides state selectivity and access to the spatial properties of the underlying orbitals.

Mixed-valence complexes containing Mn or other transition metals with spectrally well-separated core-excited states will be of future interest. A two-color scheme can then be more effectively used to access the charge migration between

0000-0003-3625-366X

metallic sites with different oxidation states and thereby reveal effects due to electronic correlations, spin transitions, vibronic couplings, and local solute—solvent interactions on the ultrafast intramolecular electron motion. ^{26–28}

In our resonant SXRS setup, spatial information on the underlying molecular orbitals was indirectly gained through the color of the X-ray pulse used. Alternatively, off-resonant, wavevector-resolved diffraction^{29,30} could be utilized, offering snapshots of the transition charge densities in time and space and providing direct access to the charge migration between different molecular sites.

■ COMPUTATIONAL DETAILS

The excited-state transition dipole matrix elements, expressed as excited-state transition density matrices, were computed using CIS-like wave functions obtained by LR-TDDFT/TDA simulations as outlined in refs 24 and 31 and implemented in a development version of the NWChem package. ^{32,33} All DFT and TDDFT computations employed the PBE0 exchange—correlation functional; ³⁴ the def2-TZVP basis set ³⁵ for C, N, H, and O; and the Sapporo-TZVP-2012 basis set ³⁶ for Mn. The system was first converged to the antiferromagnetic (*S* = 1/2) ground state before excited states were computed. A total of 100 excitations for each excited-state manifold were considered. All TDDFT-based K-edge XANES were computed with the restricted-window approach ^{37,38} as implemented in NWChem. No shifts were applied to the TDDFT spectral calculations.

ASSOCIATED CONTENT

Supporting Information

The Supporting Information is available free of charge at https://pubs.acs.org/doi/10.1021/acs.jpclett.1c01190.

Sum-over-state expressions of the linear and nonlinear X-ray signals, orbital contributions to valence- and core-excited states, nonlinear SXRS spectra for a two-color scheme with narrow X-ray pulses resonant with the Mn core, derivation of the expression of the SXRS signal, and an estimation of the signal-to-background ratio (PDF)

AUTHOR INFORMATION

Corresponding Author

Shaul Mukamel — Department of Chemistry and Department of Physics and Astronomy, University of California, Irvine, California 92697, United States; orcid.org/0000-0002-6015-3135; Email: smukamel@uci.edu

Authors

Stefano M. Cavaletto — Department of Chemistry and Department of Physics and Astronomy, University of California, Irvine, California 92697, United States;
ocid.org/0000-0003-1516-7519

Daniel R. Nascimento — Physical and Computational Sciences Directorate, Pacific Northwest National Laboratory, Richland, Washington 99352, United States; Present Address: D.R.N.: Department of Chemistry, The University of Memphis, Memphis, Tennessee 38152, United States.; orcid.org/0000-0002-2126-8378

Yu Zhang — Stanford PULSE Institute, SLAC National Accelerator Laboratory, Menlo Park, California 94025, United States; Present Address: Y.Z.: Q-Chem, Inc., 6601 Owens Drive, Suite 105, Pleasanton, California 94588, United States.; orcid.org/0000-0001-7959-3213

Niranjan Govind — Physical and Computational Sciences Directorate, Pacific Northwest National Laboratory, Richland, Washington 99352, United States; orcid.org/

Complete contact information is available at: https://pubs.acs.org/10.1021/acs.jpclett.1c01190

Notes

The authors declare no competing financial interest.

ACKNOWLEDGMENTS

S.M. is a fellow of the Hagler Institute for Advanced Study at Texas A&M University. The work was primarily supported by the Chemical Sciences, Geosciences, and Biosciences division, Office of Basic Energy Sciences, Office of Science, U.S. Department of Energy (DOE) through Awards DE-SC0019484 (S.M.C. and S.M.) and KC-030103172684 (D.R.N. and N.G.). The support of the National Science Foundation (Grant CHE-1953045) is gratefully acknowledged. S.M.C. gratefully acknowledges the support of the Alexander von Humboldt foundation through the Feodor Lynen program. A portion of the research was performed at EMSL, a DOE Office of Science User Facility sponsored by the Office of Biological and Environmental Research and located at PNNL. PNNL is operated by Battelle Memorial Institute for the United States Department of Energy under DOE Contract No. DE-AC05-76RL1830.

REFERENCES

- (1) Abreu, I. A.; Cabelli, D. E. Superoxide dismutases-a review of the metal-associated mechanistic variations. *Biochim. Biophys. Acta, Proteins Proteomics* **2010**, *1804*, 263–274.
- (2) Pecoraro, V. L.; Hsieh, W.-Y. In Metal Ions in Biological Systems: Manganese and Its Role in Biological processes; Sigel, A., Sigel, H., Eds.; Marcel-Dekker, Inc.: Basel, 2000; Vol. 37; Chapter 14, pp 429–504.
- (3) Kupitz, C.; Basu, S.; Grotjohann, I.; Fromme, R.; Zatsepin, N. A.; Rendek, K. N.; Hunter, M. S.; Shoeman, R. L.; White, T. A.; Wang, D.; et al. Serial time-resolved crystallography of photosystem II using a femtosecond X-ray laser. *Nature (London, U. K.)* **2014**, *513*, 261–265.
- (4) Messinger, J.; Robblee, J. H.; Bergmann, U.; Fernandez, C.; Glatzel, P.; Visser, H.; Cinco, R. M.; McFarlane, K. L.; Bellacchio, E.; Pizarro, S. A.; et al. Absence of Mn-centered oxidation in the $S_2 \rightarrow S_3$ transition: implications for the mechanism of photosynthetic water oxidation. *J. Am. Chem. Soc.* **2001**, *123*, 7804–7820.
- (5) Han, G.; Mamedov, F.; Styring, S. Misses during water oxidation in photosystem II are S state-dependent. *J. Biol. Chem.* **2012**, 287, 13422–13429.
- (6) Beckwith, M. A.; Roemelt, M.; Collomb, M.-N.; DuBoc, C.; Weng, T.-C.; Bergmann, U.; Glatzel, P.; Neese, F.; DeBeer, S. Manganese $K\beta$ X-ray emission spectroscopy as a probe of metalligand interactions. *Inorg. Chem.* **2011**, *50*, 8397–8409.
- (7) Krausz, F.; Ivanov, M. Attosecond physics. Rev. Mod. Phys. 2009, 81, 163.
- (8) Pellegrini, C.; Marinelli, A.; Reiche, S. The physics of x-ray free-electron lasers. *Rev. Mod. Phys.* **2016**, *88*, 015006.
- (9) Duris, J.; Li, S.; Driver, T.; Champenois, E. G.; MacArthur, J. P.; Lutman, A. A.; Zhang, Z.; Rosenberger, P.; Aldrich, J. W.; Coffee, R.; et al. Tunable isolated attosecond X-ray pulses with gigawatt peak power from a free-electron laser. *Nat. Photonics* **2020**, *14*, 30–36.
- (10) Maroju, P. K.; Grazioli, C.; Di Fraia, M.; Moioli, M.; Ertel, D.; Ahmadi, H.; Plekan, O.; Finetti, P.; Allaria, E.; Giannessi, L.; et al.

- Attosecond pulse shaping using a seeded free-electron laser. *Nature* (London, U. K.) **2020**, 578, 386–391.
- (11) Bennett, K.; Zhang, Y.; Kowalewski, M.; Hua, W.; Mukamel, S. Multidimensional resonant nonlinear spectroscopy with coherent broadband x-ray pulses. *Phys. Scr.* **2016**, *T169*, 014002.
- (12) Healion, D.; Zhang, Y.; Biggs, J. D.; Govind, N.; Mukamel, S. Entangled valence electron-hole dynamics revealed by stimulated attosecond x-ray Raman scattering. *J. Phys. Chem. Lett.* **2012**, *3*, 2326–2331
- (13) Biggs, J. D.; Zhang, Y.; Healion, D.; Mukamel, S. Watching energy transfer in metalloporphyrin heterodimers using stimulated X-ray Raman spectroscopy. *Proc. Natl. Acad. Sci. U. S. A.* **2013**, *110*, 15597–15601.
- (14) Biggs, J. D.; Zhang, Y.; Healion, D.; Mukamel, S. Multidimensional X-ray spectroscopy of valence and core excitations in cysteine. *J. Chem. Phys.* **2013**, *138*, 144303.
- (15) Zhang, Y.; Biggs, J. D.; Govind, N.; Mukamel, S. Monitoring long-range electron transfer pathways in proteins by stimulated attosecond broadband x-ray Raman spectroscopy. *J. Phys. Chem. Lett.* **2014**, *5*, 3656–3661.
- (16) Teutloff, C.; Schäfer, K.-O.; Sinnecker, S.; Barynin, V.; Bittl, R.; Wieghardt, K.; Lendzian, F.; Lubitz, W. High-field EPR investigations of Mn^{III}Mn^{IV} and Mn^{II}Mn^{III} states of dimanganese catalase and related model systems. *Magn. Reson. Chem.* **2005**, *43*, S51–S64.
- (17) Rohringer, N.; Ryan, D.; London, R. A.; Purvis, M.; Albert, F.; Dunn, J.; Bozek, J. D.; Bostedt, C.; Graf, A.; Hill, R.; et al. Atomic inner-shell X-ray laser at 1.46 nanometres pumped by an X-ray free-electron laser. *Nature (London, U. K.)* **2012**, *481*, 488–491.
- (18) Kroll, T.; Weninger, C.; Alonso-Mori, R.; Sokaras, D.; Zhu, D.; Mercadier, L.; Majety, V. P.; Marinelli, A.; Lutman, A.; Guetg, M. W.; et al. Stimulated x-ray emission spectroscopy in transition metal complexes. *Phys. Rev. Lett.* **2018**, *120*, 133203.
- (19) Weninger, C.; Purvis, M.; Ryan, D.; London, R. A.; Bozek, J. D.; Bostedt, C.; Graf, A.; Brown, G.; Rocca, J. J.; Rohringer, N. Stimulated electronic X-Ray Raman scattering. *Phys. Rev. Lett.* **2013**, *111*, 233902.
- (20) Eichmann, U.; Rottke, H.; Meise, S.; Rubensson, J.-E.; Söderström, J.; Agåker, M.; Såthe, C.; Meyer, M.; Baumann, T. M.; Boll, R.; et al. Photon-recoil imaging: Expanding the view of nonlinear x-ray physics. *Science* **2020**, *369*, 1630–1633.
- (21) O'Neal, J. T.; Champenois, E. G.; Oberli, S.; Obaid, R.; Al-Haddad, A.; Barnard, J.; Berrah, N.; Coffee, R.; Duris, J.; Galinis, G.; et al. Electronic population transfer via impulsive stimulated x-ray Raman scattering with attosecond soft-x-ray pulses. *Phys. Rev. Lett.* **2020**, *125*, 073203.
- (22) Biggs, J. D.; Zhang, Y.; Healion, D.; Mukamel, S. Two-dimensional stimulated resonance Raman spectroscopy of molecules with broadband x-ray pulses. *J. Chem. Phys.* **2012**, *136*, 174117.
- (23) Andrews, D. L.; Thirunamachandran, T. On three-dimensional rotational averages. *J. Chem. Phys.* **1977**, *67*, 5026–5033.
- (24) Nascimento, D. R.; Biasin, E.; Poulter, B. I.; Khalil, M.; Sokaras, D.; Govind, N. Resonant Inelastic X-ray Scattering Calculations of Transition Metal Complexes Within a Simplified Time-Dependent Density Functional Theory Framework. *J. Chem. Theory Comput.* **2021**, *17*, 3031–3038.
- (25) Krause, M. O.; Oliver, J. H. Natural widths of atomic K and L levels, $K\alpha$ X-ray lines and several KLL Auger lines. *J. Phys. Chem. Ref. Data* **1979**, *8*, 329–338.
- (26) Biasin, E.; Fox, Z. W.; Andersen, A.; Ledbetter, K.; Kjær, K. S.; Alonso-Mori, R.; Carlstad, J. M.; Chollet, M.; Gaynor, J. D.; Glownia, J. M. Direct observation of coherent femtosecond solvent reorganization coupled to intramolecular electron transfer. *Nat. Chem.* **2018**, *13*, 343.
- (27) Cammarata, M.; Zerdane, S.; Balducci, L.; Azzolina, G.; Mazerat, S.; Exertier, C.; Trabuco, M.; Levantino, M.; Alonso-Mori, R.; Glownia, J. M.; et al. Charge transfer driven by ultrafast spin transition in a CoFe Prussian blue analogue. *Nat. Chem.* **2021**, *13*, 10–14
- (28) Barlow, K.; Johansson, J. O. Ultrafast photoinduced dynamics in Prussian blue analogues. *Phys. Chem. Chem. Phys.* **2021**, 23, 8118.

- (29) Bennett, K.; Kowalewski, M.; Rouxel, J. R.; Mukamel, S. Monitoring molecular nonadiabatic dynamics with femtosecond X-ray diffraction. *Proc. Natl. Acad. Sci. U. S. A.* **2018**, *115*, 6538–6547.
- (30) Keefer, D.; Aleotti, F.; Rouxel, J. R.; Segatta, F.; Gu, B.; Nenov, A.; Garavelli, M.; Mukamel, S. Imaging conical intersection dynamics during azobenzene photoisomerization by ultrafast X-ray diffraction. *Proc. Natl. Acad. Sci. U. S. A.* **2021**, *118*, e2022037118.
- (31) Biasin, E.; Nascimento, D. R.; Poulter, B. I.; Abraham, B.; Kunnus, K.; Garcia-Esparza, A. T.; Nowak, S. H.; Kroll, T.; Schoenlein, R. W.; Alonso-Mori, R.; et al. Revealing the bonding of solvated Ru complexes with valence-to-core resonant inelastic X-ray scattering. *Chem. Sci.* **2021**, *12*, 3713.
- (32) Valiev, M.; Bylaska, E.; Govind, N.; Kowalski, K.; Straatsma, T. P.; Van Dam, H. J. J.; Wang, D.; Nieplocha, J.; Apra, E.; Windus, T. L.; et al. NWChem: A comprehensive and scalable open-source solution for large scale molecular simulations. *Comput. Phys. Commun.* **2010**, *181*, 1477–1489.
- (33) Aprà, E.; Bylaska, E. J.; de Jong, W. A.; Govind, N.; Kowalski, K.; Straatsma, T. P.; Valiev, M.; van Dam, H. J. J.; Alexeev, Y.; Anchell, J.; et al. NWChem: Past, present, and future. *J. Chem. Phys.* **2020**, *152*, 184102.
- (34) Adamo, C.; Barone, V. Toward reliable density functional methods without adjustable parameters: The PBE0 model. *J. Chem. Phys.* **1999**, *110*, 6158–6170.
- (35) Weigend, F.; Ahlrichs, R. Balanced basis sets of split valence, triple zeta valence and quadruple zeta valence quality for H to Rn: Design and assessment of accuracy. *Phys. Chem. Chem. Phys.* **2005**, *7*, 3297
- (36) Noro, T.; Sekiya, M.; Koga, T. Segmented contracted basis sets for atoms H through Xe: Sapporo-(DK)-nZP sets (n = D, T, Q). *Theor. Chem. Acc.* **2012**, *131*, 1124.
- (37) Lopata, K.; Van Kuiken, B. E.; Khalil, M.; Govind, N. Linear-Response and Real-Time Time-Dependent Density Functional Theory Studies of Core-Level Near-Edge X-Ray Absorption. *J. Chem. Theory Comput.* **2012**, *8*, 3284–3292.
- (38) Zhang, Y.; Biggs, J. D.; Healion, D.; Govind, N.; Mukamel, S. Core and valence excitations in resonant X-ray spectroscopy using restricted excitation window time-dependent density functional theory. *J. Chem. Phys.* **2012**, *137*, 194306.